PRX QUANTUM **4,** 020317 (2023)

Editors' Suggestion

Controlling Two-Dimensional Coulomb Crystals of More Than 100 Ions in a Monolithic Radio-Frequency Trap

Dominik Kiesenhofer,[1,2] Helene Hainzer,[1,2] Artem Zhdanov,[1] Philip C. Holz,[3] Matthias Bock,[1,2] Tuomas Ollikainen,[1,2] and Christian F. Roos[1,2,*]

[1] *Institut für Experimentalphysik, Universität Innsbruck, Technikerstraße 25, 6020 Innsbruck, Austria*
[2] *Institut für Quantenoptik und Quanteninformation, Österreichische Akademie der Wissenschaften, Technikerstraße 21a, 6020 Innsbruck, Austria*
[3] *Alpine Quantum Technologies GmbH, Technikerstraße 17/1, 6020 Innsbruck, Austria*

(Received 2 February 2023; accepted 6 April 2023; published 28 April 2023)

Linear strings of trapped atomic ions held in radio-frequency (rf) traps constitute one of the leading platforms for quantum simulation experiments, allowing the investigation of interacting quantum matter. However, linear ion strings have drawbacks, such as the difficulty of scaling beyond approximately 50 particles as well as the inability to naturally implement spin models with more than one spatial dimension. Here we present experiments with planar Coulomb crystals of up to 105 $^{40}\mathrm{Ca}^+$ ions in a novel monolithic rf trap, laying the groundwork for quantum simulations of two-dimensional spin models with single-particle control. We characterize the trapping potential by analysis of crystal images and compare the observed crystal configurations with numerical simulations. We further demonstrate stable confinement of large crystals, free of structural configuration changes, and find that rf heating of the crystal is not an obstacle for future quantum simulation experiments. Finally, we prepare the out-of-plane motional modes of planar crystals consisting of up to 105 ions close to their ground state by electromagnetically induced transparency cooling, an important prerequisite for implementing long-range entangling interactions.

DOI: 10.1103/PRXQuantum.4.020317

I. INTRODUCTION

Models of interacting quantum many-body systems are often easy to write down but hard to study by analytical or numerical techniques. Quantum simulation embodies the concept that experiments with engineered quantum systems might provide novel insights into quantum many-body physics, making it an important application of noisy intermediate-scale quantum processors [1]. To this end, the experimental system can be directly engineered for realization of the desired interactions, or sequences of quantum gates can be used for approximation of the dynamics in a controlled way [2], referred to as "analog quantum simulation" and "digital quantum simulation," respectively. Furthermore, entangling interactions may be used as a resource for variational methods [3].

Various experimental platforms have been suggested to realize a quantum simulator—neutral atoms in optical lattices [4], trapped ions [5], Rydberg atom arrays [6], superconducting circuits [7,8], and photonic waveguide arrays [9,10], to name a few. Trapped atomic ions are among the most precisely controllable quantum systems available for applications such as quantum computation [11,12], metrology and sensing [13–15], and simulation [5,16]. In particular, in analog and variational quantum simulation experiments, control over large ion crystals has proven possible, allowing the study of quantum many-body physics phenomena with several tens of particles [17–20]. Scaling up trapped-ion experiments to a larger number of individually controllable particles is, however, challenging. Radio-frequency (rf) traps such as linear Paul traps have enabled complete quantum control of up to 50 ions in linear chains [21]. In these state-of-the-art trapped-ion experiments, entangling interactions are mediated across the system by lasers coupling to the collective motional modes of the ion crystal, while coherent single-particle operations are achieved by addressing individual ions with tightly focused laser beams. Keeping a long one-dimensional crystal linear, however, requires extremely anisotropic trapping potentials [22,23], eventually limiting the number of ions that can be controlled with high fidelity. Problems in laser cooling arise from the fact that the ions are only weakly confined in the axial direction of the string,

---

[*] christian.roos@uibk.ac.at

resulting in high heating rates of the axial motional modes. In addition, the spatial extent of long linear ion chains leads to difficulties in laser-addressing the outer ions.

One obvious approach to scaling up trapped-ion architectures is to use a second spatial dimension. While Penning traps offer the possibility to work with hundreds of ions in a planar configuration [24], single-ion control has not yet been implemented in the laboratory as crystals in Penning traps rotate at rates of tens to hundreds of kilohertz about the out-of-plane axis [25]. Surface trap arrays, where each rf microtrap confines a single ion, would, in principle, allow ions to be trapped in nearly arbitrary two-dimensional (2D) geometries, but so far this has been achieved only in small systems of several ions [26–28]. Here, substantial technical challenges need to be overcome: Surface traps suffer from low trap depths and are thus prone to ion loss. Furthermore, for the realization of entangling interactions mediated by the ions' motion, the ions need to be brought sufficiently close together (on the order of tens of micrometers) to produce an interaction on timescales much faster than the ions' coherence time. This is possible only by bringing the ions close to the trap electrodes and thus subjecting them to strong surface electric field noise, leading to high heating rates that limit the motional coherence. Lastly, free-space optical access is challenging for large chip traps, creating an additional technological overhead for optics integration.

Alternatively, it is possible to confine ions in a planar configuration in the potential of a single rf trap, which is an approach recently taken by several groups around the world [29–32] and also the one taken for the experiment described in this article. While this approach allows harnessing of the many benefits that linear ion strings provide, such as tunable-range entangling interactions, ranging from all-to-all to nearest-neighbor couplings, spin models can be implemented in two dimensions on top of that. On the downside, there are difficulties to be overcome: Most ions in a planar crystal experience rf-driven micromotion, as they are inevitably displaced from the rf null. Any laser used to manipulate these ions will appear to be phase modulated at the trap drive frequency. However, adverse effects on the laser-ion interactions, which form the basis of laser cooling and coherent operations, can be suppressed to first order by application of laser beams only from directions perpendicular to the micromotion. This potentially opens up another challenge: the necessity to develop novel ion-trap geometries so as to gain optical access from relevant directions. With such a trap design, promising results were presented recently, such as electromagnetically induced transparency (EIT) cooling of the out-of plane motional modes of a 2D crystal consisting of 12 $^{171}\mathrm{Yb}^{+}$ ions [33] and frustrated quantum magnetism with ten ions [34]. However, it remains to be shown that these results can be extended to experiments with considerably larger crystals, which face additional challenges: rf heating of the ions could compromise entangling interactions mediated by ground-state cooled collective modes of motion. Furthermore, planar ion crystals can display various distinct lattice configurations. Transitions between these crystal configurations can be initiated, for example, by background gas collisions or by rf heating [35,36]. The number of such configuration changes needs to be minimized as single-ion quantum state detection and control rely on stable ion positions.

In this article we present an ion-trap apparatus designed for quantum simulation experiments with individually controllable particles in a 2D configuration. We demonstrate quantum control over planar ion crystals of up to 105 ions and provide experimental evidence that crystal lattice configuration changes and rf heating are not obstacles for quantum simulation experiments with these crystals. The paper is structured as follows: In Sec. II, we introduce our novel monolithic linear Paul trap, and describe our approach to loading, cooling, quantum-state manipulation, and readout of planar $^{40}\mathrm{Ca}^{+}$ ion crystals. In Sec. III, we analyze the planarity and orientation of the ion crystals, characterize the trapping potential, investigate the stability of the lattice configurations, measure the heating dynamics of the ion crystals, and demonstrate EIT cooling of the out-of-plane modes of a small (eight ions) and a large (105 ions) 2D ion crystal—the largest ion crystal held in a rf trap that has successfully been cooled close to the ground state. Our findings are summarized in Sec. IV.

II. APPARATUS

In a standard linear Paul trap, consisting of two rf blades, two dc blades, and two endcap electrodes, planar crystals can be trapped either in the plane spanned by the two radial directions or in a plane spanned by one radial direction and the axial direction, as illustrated in Figs. 1(a) and 1(b), respectively. The necessary condition for the formation of a planar crystal is given by $\omega_s/\omega_w > 1.23N^{1/4}$ [23], where ω_s is the secular frequency in the direction of strong confinement, in which the crystal is squeezed flat, ω_w is the frequency in the directions of weak confinement, in which the crystal is extended, and N is the number of ions. The required asymmetry of the trap frequencies can be achieved by introducing dc voltages on the dc and endcap electrodes to squeeze the crystal into the desired plane.

In terms of the rf-power requirements, neither of the crystal orientations provides an advantage compared with the other one (see Appendix A). However, it is beneficial to choose the orientation shown in Fig. 1(b) because rf-driven micromotion occurs only along a single direction. In this case an entire plane is available from which the ions can be addressed with laser beams perpendicular to the micromotion, therefore eliminating the adverse effects on laser-ion interactions to the first order.

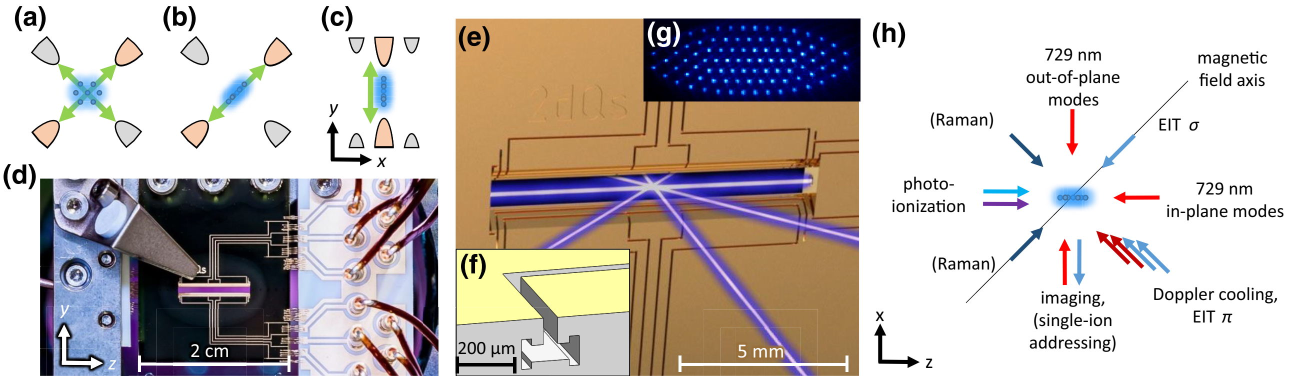

FIG. 1. (a),(b) Radial cross section of a linear Paul trap. The orange (gray) shapes symbolize rf (dc) electrodes. The green arrows denote the directions of micromotion experienced by the ions in the crystal (blue). In (a), the planar crystal is oriented in the plane spanned by the radial directions of the trap, and in (b), it is oriented in the plane spanned by one radial direction and the axial direction. (c) Radial cross section of a three-layer trap. This geometry allows optical access perpendicular to micromotion. (d) Photograph of the ion trap inside the vacuum chamber. The trap chip is seen in the center of the picture. Ions are loaded from a calcium target, attached to a funnel aperture (top left). Two printed circuit boards made of alumina (front right and rear left of the trap chip) provide interfaces between gold wirebonds to the trap electrodes and cables to the vacuum feedthroughs. (e) Three-dimensional rendering of the central region of the ion trap (rear side with rf electrode leads) and laser beams in the horizontal plane. (f) The trench geometry, used to electrically isolate electrodes. The electrode separation on the surface of the trap chip is 50 µm. (g) A Coulomb crystal consisting of 91 $^{40}\text{Ca}^+$ ions stored in the center of the trap. (h) Top view of the laser beam and magnetic field geometry in the horizontal plane. Parentheses indicate beams that have not yet been implemented. Not shown are two laser beams that do not lie within the horizontal plane: a 729-nm beam for spectroscopy of in-plane and out-of-plane motional modes that has an angle of 45° with the horizontal plane, and a second cooling beam at an angle of approximately 20° with the horizontal plane coupling also to the vertical direction.

We therefore choose the crystal orientation illustrated in Fig. 1(b), and modify the standard linear Paul trap geometry as shown in Fig. 1(c), to gain optical access from relevant directions for laser cooling and manipulation, and in particular perpendicular to the crystal plane for ion imaging and laser-addressing of individual ions. The price to pay for having a micromotion-free optical access in an entire plane is a slightly increased sensitivity of the trap potential anisotropy with respect to rf-voltage fluctuations (see Appendix A), which can be mitigated by a state-of-the-art active stabilization of the rf voltage.

In the following, we provide a detailed description of our linear Paul trap and overall apparatus for experiments with planar crystals of $^{40}\text{Ca}^+$ ions.

A. A novel monolithic linear Paul trap

Effectively, our electrode geometry, shown in Fig. 1(c), realizes a three-layer trap [37]. It differs from a standard linear Paul trap in that the dc blades are split and projected to the top and bottom. The distance between the rf electrode and the trap center is 400 µm. The dc electrodes are recessed with respect to the rf electrode to allow additional optical access at 45° angles from the top and the bottom. Furthermore, these electrodes are segmented as shown in Fig. 1(e). The outer segments represent the endcap electrodes and allow axial confinement. Additional ground electrodes are introduced between the rf and dc electrodes. Their purpose is to reduce rf field components in the axial trap direction introduced by the gaps between dc segments, which can lead to unwanted micromotion of the ions along that direction. More details can be found in Appendix B.

While machined and hand-assembled linear Paul traps have led to state-of-the-art experiments with one-dimensional ion crystals, small alignment imperfections could lead to difficulties in working with large 2D ion crystals. A misalignment of the trap electrodes with respect to each other could, on the one hand, enhance nonlinear resonances in the trapping potential, which can lead to the ejection of ions from the trap [38,39], an effect that increases in severity the further an ion is displaced from the rf null [40]. On the other hand, a misalignment could lead to increased micromotion in directions that cannot be effectively compensated. Therefore, we design a monolithic ion trap allowing precise electrode arrangements without the need for hand assembly. The trap is shown in Fig. 1(d). Figure 1(e) displays a rendering of the central trap region with laser beams representing the directions used for optical access in the x-z (horizontal) plane. Holes in the trap chip enable laser access from the axial direction. Planar ion crystals are trapped in the y-z plane; an example comprising 91 ions is shown in Fig. 1(g).

The trap is microfabricated [41] via selective laser-induced etching [42–45]. In the first stage of the manufacturing process, the design is written into a fused-silica wafer with a pulsed laser, locally changing the properties of the glass. The illuminated material is etched in a bath of hydrofluoric acid in the second stage. With use of this approach it is possible to realize electrode structures with submicrometer precision, and, in particular, to create trenches that extend underneath the surface of the chip [42,46]. After metallization (sputtering of 30-nm titanium and 3-μm gold), the trenches with undercuts, shown in Fig. 1(f), keep the electrodes electrically isolated.

The ion trap is operated at rf voltages of approximately 1 kV peak to peak and with a frequency Ω_{rf} of $2\pi \times 43.22$ MHz to ensure a Mathieu stability parameter $q \lesssim 0.1$ and, thus, a low level of micromotion. In the experiments presented in this article, the crystals are trapped in a potential with secular oscillation frequencies $\omega_s/2\pi$ of approximately 2.2 MHz in the strongly confining direction and a few hundred kilohertz in the two weakly confining directions. The rf power is actively stabilized to ensure stability of the confinement on both long and short timescales. More details on control and stability of the trap rf can be found in Appendix B 2.

Since the principal axes of the trap potential are well aligned with the trap's geometrical axes, x, y, and z, the secular frequencies are henceforth denoted as ω_x, ω_y, and ω_z, respectively, where x is the direction perpendicular to the ion crystal plane.

B. Laser beam and magnetic field geometry

Figure 1(h) provides a schematic overview of the geometry of the laser beams and the magnetic field in our apparatus. The quantization axis is defined via permanent magnets, creating a magnetic field that is parallel to the x-z plane and has an angle of 45° with respect to the crystal plane. Additionally, a pair of coils in anti-Helmholtz configuration along the same direction is used to compensate unwanted magnetic field gradients.

We use eight directions for optical access in the x-z plane, which is perpendicular to the direction of micromotion, and thus allows micromotion-free laser-ion interaction. Along x, an objective lens, with a numerical aperture of 0.289, is used to collect fluorescent light at 397 nm from the ions for imaging and state readout. The light is guided and focused onto the chip of an electron-multiplying CCD camera and a photomultiplier tube (PMT). Two photoionization beams are focused through the axial holes of the trap (along z). The ions are Doppler-cooled from a direction orthogonal to the quantization axis, from which the light field can couple to all in- and out-of-plane motional modes with the exception of the center-of-mass mode along y. However, we find that ion crystals can still be cooled efficiently in all three directions, with the exception of small crystals of several ions, or single ions, for which we use a different cooling beam that has an overlap with the y direction [20° angle with the horizontal plane, not shown in Fig. 1(h)]. Ground-state preparation of the out-of-plane motional modes by means of EIT cooling is done with two beams: one circularly polarized propagating along the quantization axis, and one linearly polarized propagating perpendicular to it. Coherent operations on the optical qubit transition at 729 nm are implemented with beams along the x direction and the z direction. These beams can also be used to couple to the out-of-plane motional modes, or the in-plane modes, respectively. Moreover, a 729-nm beam at an angle of 45° with the horizontal plane (not shown) couples to both the in-plane and the out-of-plane motional modes.

The beams labeled in parentheses in Fig. 1(h) are not yet implemented in our setup. In the future we aim to realize entangling interactions by coupling to the out-of-plane motional modes with bichromatic Raman laser beams at 396 nm. These will propagate along and perpendicular to the quantization axis, respectively, opposite to the EIT cooling beams. Additionally, we plan to use the objective lens to tightly focus laser beams at 729 nm for addressing of individual ions.

C. Loading and cooling

Ions are loaded via laser ablation using a 515-nm pulsed laser. The power of the ablation pulses can be precisely controlled via a motorized wave plate in combination with a polarizing beam splitter and is set low enough such that mostly neutral atoms are ablated from the calcium target. For isotope-selective photoionization of ^{40}Ca, we use a two-stage process: A 422-nm laser drives a cycling transition to a highly excited state, from which the valence electron is detached by laser light with a wavelength of 375 nm. In the trap center, the atomic beam and the photoionization beams cross at an angle of 45°, which allows the exploitation of the Doppler shift to select slower atoms from the velocity distribution.

Deterministic loading of single ions and large crystals with a desired ion number is typically realized on a timescale of less than 1 min by combining control over ablation laser power (to add ions to the crystal) and control over the trapping potential depth (to remove ions from the crystal).

Doppler cooling is performed on the $4S_{1/2} \leftrightarrow 4P_{1/2}$ dipole transition at 397 nm, with two repumper lasers at 854 and 866 nm, which remove population from the long-lived D states. Further cooling of the ions to the motional ground state is possible via either sideband cooling or EIT cooling. For EIT cooling, we use 397-nm light that is blue-detuned by 110 MHz from the $4S_{1/2} \leftrightarrow 4P_{1/2}$ transition, as discussed in more detail in Sec. III E.

D. Qubit manipulation

Qubits can be encoded in the two Zeeman states of the $4S_{1/2}$ ground-state manifold (ground-state qubit) or in one of the two ground states in combination with one of the metastable $3D_{5/2}$ Zeeman states (optical qubit). We couple the ground states coherently via a magnetic rf field, oscillating at approximately 11 MHz, which is generated via a coil placed outside the vacuum. We enclose our apparatus in a magnetic field shielding, and obtain a coherence time of about 130 ms for the ground-state qubit via Ramsey experiments. A standard spin-echo pulse sequence extends the ground-state coherence time to about 370 ms.

The optical qubit is manipulated with a frequency-stable laser at 729 nm with a linewidth of approximately 1 Hz to realize coherent operations on the electronic $4S_{1/2} \leftrightarrow 3D_{5/2}$ quadrupole transition. To distinguish the two qubit states, we use the electron-shelving technique: Ions are excited on the $4S_{1/2} \leftrightarrow 4P_{1/2}$ transition and their fluorescence is detected via the PMT and imaged onto the electron-multiplying CCD camera. An ion appears bright or dark, depending on whether the electron is projected onto the $4S_{1/2}$ state or the $3D_{5/2}$ state of the optical qubit. We map the ground-state qubit to the optical qubit using 729-nm light, and use the same readout technique.

E. Quantum state analysis

Data analysis for a system comprising more than one ion relies on ion-specific readout of bright and dark states from camera images. Here, a high-fidelity distinction between the qubit states, even for short detection times of a few milliseconds, is crucial. In the case of 2D crystals, this becomes even more challenging than for linear ion chains, as the ions can suffer from higher levels of light scattering crosstalk due to the increased number of neighboring ions.

Our algorithm for quantum state analysis will be presented in detail in a forthcoming publication. Here we provide just a short summary: The general idea is to first take a set of reference images, at the beginning of the experiment, where the ions are randomly bright and dark. Next, we use statistical tools to obtain projection matrices that can be multiplied to an image yielding the pseudocounts for each ion, being free of crosstalk counts from neighboring ions.

III. SYSTEM CHARACTERIZATION

Our apparatus is capable of trapping stable planar crystals of up to $N \approx 100$ ions. Via the dc electrodes of the ion trap, we introduce an anisotropy in the weak directions of the trapping potential to create ion crystals that are elongated along the axial trap direction. These elliptically shaped crystals have a stabler crystal lattice structure compared with round ones, in particular due to a suppression of librational modes. We observe crystal lifetimes of several hours or even days, limited only by the occurrence of a “dark ion.” This can be either a different atomic species, other than $^{40}\mathrm{Ca}^+$, which is caught in the trapping potential, or a molecular ion, formed in a chemical reaction between $^{40}\mathrm{Ca}^+$ and the residual background gas. To quantify the achievable control over ions in our setup and assess the suitability of our platform for future quantum simulation experiments, characterization measurements are performed. We investigate the planarity, orientation, heating dynamics, crystal lattice stability, and ground-state cooling of large 2D ion crystals, as well as the trap potential anharmonicity by analysis of crystal images.

A. Planarity and crystal orientation

To ensure the planarity and optimum alignment of an ion crystal in the trap center, we probe the sideband-resolved $4S_{1/2} \leftrightarrow 3D_{5/2}$ transition. We determine the out-of-plane micromotion modulation index β_{OOP} of the individual ions by measuring the micromotional sideband Rabi frequency Ω_{sb} and the respective carrier Rabi frequency Ω_{carr} with a laser beam whose incidence is normal to the plane in which we confine the crystal. In the limit of small modulation, we have $\beta_{\mathrm{OOP}} \approx 2\Omega_{\mathrm{sb}}/\Omega_{\mathrm{carr}}$. In Fig. 2, the measured modulation indices of individual ions in a 91-ion crystal and a 105-ion crystal are shown. When the crystal is in an optimum position in the center of the trap we expect the modulation indices to be minimized. However, several imperfections can arise, such as the ions not being confined in a single plane, or the crystal plane being misaligned with respect to the trap center or tilted with respect to the principal axes. In Fig. 2(a), we investigate the planarity of a 91-ion crystal. In this example, the confinement in the x (out-of-plane) direction is too low and, consequently, the ions in the center of the crystal display a higher micromotion modulation index as they are pushed out of the crystal plane. This can be resolved by increasing the voltages applied to the middle segments of the ion-trap dc electrodes.

Figures 2(b)–2(e) display the micromotion modulation indices for 105-ion planar crystals. Figures 2(b)–2(d) show examples where the crystals are not optimally positioned and oriented in the trap center. Here we observe tilts and shifts, reflected in a higher level of micromotion for certain ions. Such tilts or shifts can be a consequence of asymmetries in the trap geometry as well as stray fields (e.g., from dust particles). However, we can compensate for these by applying asymmetric voltages on the outer segmented electrodes of the trap, to tilt and translate the crystal in all three dimensions and move it into the optimum position in the trap center. In this case—combined with applying enough voltage to the middle segments to ensure planar crystals—we end up with the well-compensated crystal shown in Fig. 2(e), where $\beta_{\mathrm{OOP}} < 0.02$ for all ions. The slightly increased modulation indices of the outer ions likely stem from a small misalignment of either the laser beam or the ion crystal, such that the beam is not perfectly perpendicular to the crystal plane. However, these effects are small, reflected in the overall low modulation indices, and do not restrict the planned experiments. For the optimally placed 2D crystals, we measure the

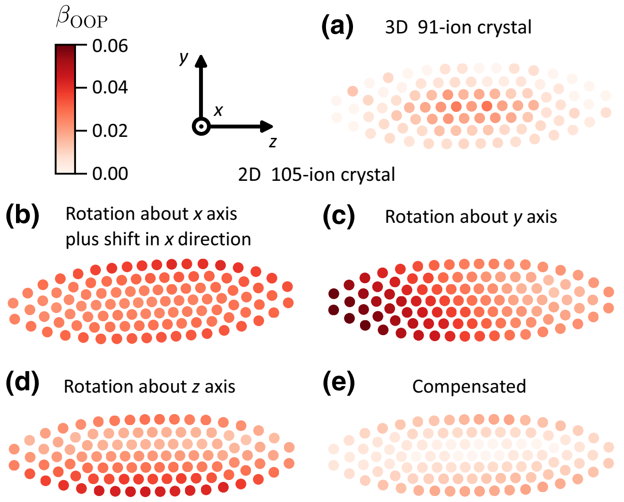

FIG. 2. Measurement of the micromotion modulation index in the out-of-plane direction. (a) A 91-ion crystal is used to investigate planarity. In this example, ions in the center of the crystal display a higher modulation index as they are pushed out to the third dimension. (b)–(d) Examples of planar 105-ion crystals displaying various undesirable scenarios where shifts along and rotations about arbitrary axes are present, leading to increased micromotion modulation indices. The labels indicate the main contribution to the crystal misalignment. (e) By applying precalculated sets of dc voltages, we are able to compensate for shifts and rotations and align the ion crystal with the trap center and principal axes such that the micromotion modulation indices are minimized for all ions.

oscillation frequencies $\omega_x = 2\pi \times 2196$ kHz, $\omega_y = 2\pi \times 680$ kHz and $\omega_z = 2\pi \times 343$ kHz for the 91-ion crystal and $\omega_x = 2\pi \times 2188$ kHz, $\omega_y = 2\pi \times 528$ kHz, and $\omega_z = 2\pi \times 248$ kHz for the 105-ion crystal. We have not yet made attempts to create planar crystals with ion numbers beyond 105 but believe that achieving planarity and lattice stability for larger crystals will at some point become challenging. On the one hand, the maximum rf voltage that can be applied to the ion trap is limited. On the other hand, lowering the confinement in the weak directions to maintain the ratio of trap frequencies required for achieving planarity will eventually become problematic.

B. Crystal shape

A planar crystal trapped in a harmonic potential with anisotropy takes on an elliptical shape. The latter is quantified by the crystal's aspect ratio $\zeta = a_2/a_1$, defined as the length ratio of the semiminor axis a_2 and the semimajor axis a_1. When one is conducting numerical simulations of ion positions in a given harmonic potential, knowledge of ζ is helpful for starting the simulation with a good initial guess of the ion positions. However, there is no simple relation linking ζ to the trapping frequencies. We determine ζ in the following way: We calculate the covariance matrix C of the ion positions (y_i, z_i), which can be precisely measured by recording the ions' fluorescence on a CCD camera [47]. Diagonalization of C yields $\zeta = \sqrt{\lambda_2/\lambda_1}$, where λ_1 and λ_2 ($\lambda_1 \geq \lambda_2$) are the two eigenvalues of C. In a harmonic potential characterized by its trap anisotropy

$$\xi = \omega_y/\omega_z, \tag{1}$$

one finds $\zeta \leq \xi^{-1}$. For sufficiently large ion numbers, the crystal can be modeled as a charged fluid, the shape of which can be calculated from potential theory [48]. Then ζ is related to ξ via

$$\zeta^2 \frac{K - E}{E - \zeta^2 K} = \xi^{-2}, \tag{2}$$

where $K = K(\sqrt{1-\zeta^2})$ and $E = E(\sqrt{1-\zeta^2})$ are complete elliptic functions of the first and second kinds [see Eq. (3.81) in Ref. [49]].

We apply this method for a measurement of the aspect ratio to a 91-ion crystal. From sideband spectroscopy of the $4S_{1/2} \leftrightarrow 3D_{5/2}$ transition, the secular oscillation frequencies are determined to be $\omega_y = 2\pi \times 742$ kHz and $\omega_z = 2\pi \times 370$ kHz, yielding $\xi^{-1} = 0.499$. From the ion positions we find an aspect ratio ζ of 0.382, in good agreement with $\zeta_{\mathrm{th}} = 0.403$ predicted by Eq. (2).

C. Characterization of the trapping potential from crystal images

The analysis of planar crystal images is not limited to determining the anisotropy of the trapping potential via Eq. (2), but yields much more information, such as trapping frequencies and possible anharmonicities of the potential. The ions' equilibrium positions in a crystal are determined by a balance between the confining force of the trap potential and the repelling Coulomb force between the ions. For a planar crystal, we can calculate the Coulomb forces between the ions from their observed positions and, therefore, deduce the force that is exerted by the trapping potential. Assuming a harmonic trapping potential

$$V = \frac{1}{2}\begin{pmatrix} z - z_0, & y - y_0 \end{pmatrix} A \begin{pmatrix} z - z_0 \\ y - y_0 \end{pmatrix}, \tag{3}$$

where

$$A = \begin{pmatrix} \alpha & \gamma \\ \gamma & \beta \end{pmatrix}$$

is a symmetric matrix, V is determined from a fit after calculation of the Coulomb force components in the two directions spanning the crystal plane [vertical (y) and horizontal (z) on the camera image]. Figure 3(a) shows the Coulomb force field that we deduce from an image analysis of a 91-ion crystal. The eigenvalues of A are proportional to the squares of the secular oscillation frequencies in the crystal plane. Taking the square root of

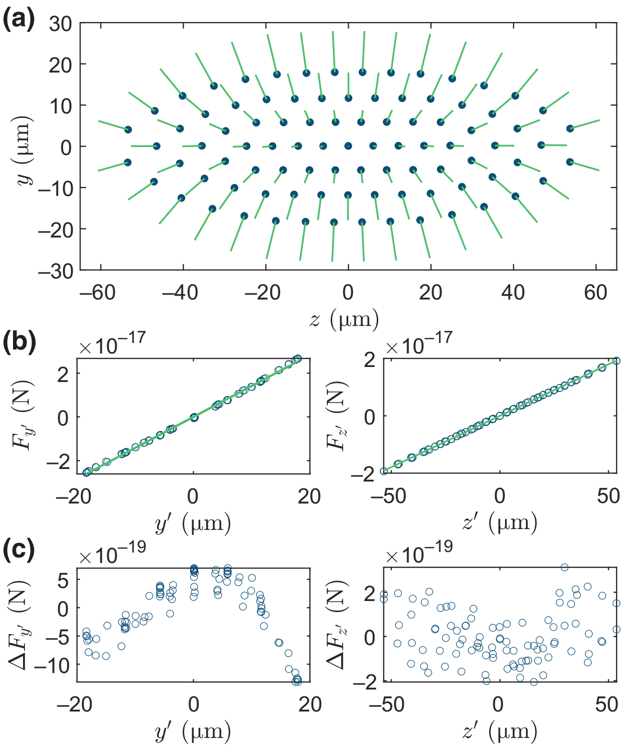

FIG. 3. Characterization of the trapping potential from an image of a 91-ion planar crystal. (a) The blue points indicate the positions of the individual ions, and green lines represent the forces exerted on the ions (arbitrary units). (b),(c) Force components $F_{y'}$ and $F_{z'}$ and their residuals $\Delta F_{y'}$ and $\Delta F_{z'}$ (with respect to the linear fit) along the two directions y' and z' of the rotated coordinate system.

the ratio of these oscillation frequencies, we find a potential anisotropy ξ^{-1} of 0.503, in good agreement with the result ($\xi^{-1} = 0.499$) obtained from sideband spectroscopy reported in Sec. III B. The principal axes of V are not necessarily aligned with the coordinate system (z, y) of the imaging system. For this reason, we introduce a rotated coordinate system defined by $z' = z\cos\phi + y\sin\phi$ and $y' = -z\sin\phi + y\cos\phi$. The fit of V yields $\phi = 0.004$, showing that both coordinate systems nearly coincide for this crystal. In Fig. 3(b), we plot the Coulomb force components $F_{y'}(z'_i, y'_i)$ and $F_{z'}(z'_i, y'_i)$ along the principal axes; the residuals $\Delta F_{y'}$ and $\Delta F_{z'}$ from a linear fit are shown in Fig. 3(c). These residuals reveal that the trapping potential is not purely harmonic. However, as the deviations from the linear fit are small, we conclude that anharmonic contributions to the trapping potential are rather minor. The determination of the Coulomb forces in physical units as presented in Fig. 3 necessitates a calibration of the imaging system, which we obtain by matching the value of the secular frequency ω_z found by crystal image analysis to the value obtained by sideband spectroscopy. By doing this, we find a magnification factor of 22.4 in our imaging system.

Once the magnification of the imaging system has been precisely calibrated, image analysis of planar ion crystals might enable measurement of the dependence of the potential curvatures on changes of particular dc trap voltages much faster than approaches based on sideband spectroscopy.

D. Crystal configurations and stability

Langevin collisions of the ions with atoms and molecules of the residual background gas can induce a transition to a noncrystalline (melted) phase in which energy can be transferred from the trapping rf field to the ions in the cloud [50,51]. A melted crystal prevents any further quantum measurement. Hence, during an experimental sequence it is essential that the ion crystal maintains its crystalline structure, which we verify with quantitative measurements described in the following subsection.

Furthermore, lower-energy collisions can initiate transitions between distinct configurations of the crystalline structure of a planar ion crystals held at a fixed trap potential. This phenomenon is, for example, well known for a zigzag crystal with two mirror-symmetric degenerate configurations at minimum potential energy [35,52]. For larger, less elongated 2D ion crystals, we observe an increasing number of distinct crystal configurations. We analyze those by recording image series of the ion crystal as described below. With this tool we are able to detect, minimize, and filter out the occurrence of metastable lattice configurations during experimental data taking, which is critical as individual-ion readout and laser addressing rely on stable ion positions.

1. Melting and recrystallization

When a melting event occurs, fewer photons are scattered by the nonlocalized, hot ions during Doppler cooling. The resulting fluorescence count drop on the PMT is used to automatically detect these events during the measurement sequences and trigger immediate recrystallization of the ions. For this purpose, a far-red-detuned ($\Delta = 2\pi \times 330$ MHz) Doppler cooling beam is used for 100 ms along with the primary Doppler cooling beam. We quantify the time it takes planar ion crystals consisting of 8, 54, and 91 ions to melt into an ion cloud in the absence of any laser cooling in the following way: Cooling beams are turned off for a variable waiting time, after which fluorescence counts are recorded with the PMT. These counts allow a distinction between crystalline and noncrystalline phases. Afterwards, Doppler cooling and recrystallization beams are turned on for 100 ms to retrieve the crystalline structure of the ions. At the end of the cycle, a camera image is taken to ensure that the ions are recrystallized before the next measurement. Figure 4 shows the percentage of measurements in which an ion crystal survives in crystalline form as a function of the waiting time. The time it takes

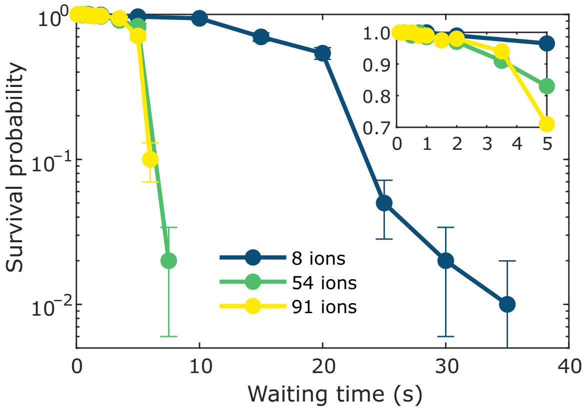

FIG. 4. Melting behavior of planar crystals. Shown here is the probability that a crystal consisting of a certain number of ions has not melted into a cloud after a waiting time without any laser cooling. For each data point, 100 experiments are performed. The inset shows the probabilities for short waiting times in more detail.

for an eight-ion crystal to be melted in 100% of cases is approximately 40 s. For larger crystals the melting events occur on a shorter timescale, but still the ions remain in the crystalline phase with high probability even after several seconds. Assuming only Langevin collisions as the cause of melting, one would expect a purely exponential behavior as a function of time. We interpret the observed nonexponential decay and the nonlinear dependence on the ion number as evidence that these melting events are not exclusively caused by collisions with residual background gas, but are possibly caused by a combination of collisions followed by rf-induced heating. Simulations reported in Ref. [54] suggest a q^4 dependence of rf heating. Thus, the low $q \approx 0.1$ in our experiment mitigates rf-heating effects, but for the long timescales investigated here, these effects become relevant. Regardless of the mechanism behind the melting events, the observed crystal survival time of several seconds for larger crystals is long compared with the time of the envisaged experimental sequences.

A further experiment is performed to estimate the time it takes to recrystallize an ion cloud after the occurrence of a melting event. Here, cooling lasers are switched off for a waiting time of 1 s. This represents an upper limit for planned experiments and, thus, mimics a realistic timescale for the free evolution time of the ion cloud before the recrystallization pulse is applied. After 1 s, the ions' fluorescence is measured by the PMT to determine whether the ion crystal has melted. We investigate a 91-ion planar crystal, for which melting within a waiting time of 1 s occurs in approximately 1% of cases, consistent with the data provided in Fig. 4. When a melting event is detected, a recrystallization pulse of variable length is applied before an image of the ions is taken to check if the recrystallization was successful. For this crystal we observe recrystallization after 70 ms in 101 of 102 observed melting events. Hence, a pulse duration of 100 ms is sufficient to recrystallize a cloud after a melting event is detected within a measurement sequence.

2. Crystal configuration analysis

To detect distinct crystal lattice configurations, we record a series of N_P images taken approximately 0.5 s apart, with $N_P \approx 10^4$. Every image j is represented as a column vector $\mathbf{x}_j$ of pixel brightness values and is stored in a matrix $M = [\mathbf{x}_1 \mathbf{x}_2 \dots \mathbf{x}_{N_P}]$, where columns and rows correspond to individual images and pixels, respectively. A dimensionality reduction is achieved by means of a principal component analysis of M, yielding a number of "eigenpictures" $\mathbf{y}_i$ that correspond to the eigenvectors of the largest eigenvalues of the covariance matrix $Q = MM^T$.

These eigenpictures provide a basis that enables a faithful representation of any image $\mathbf{x}_j \approx \sum_{i=1}^{n} c_{ij} \mathbf{y}_i$, where $c_{ij} = \mathbf{y}_i^T \mathbf{x}_j$, with use of only a small number n of eigenpictures. In this way, every picture can be represented by a set of n numbers. We empirically find that $n \leq 8$ is sufficient for distinguishing different crystal configurations in our experiments. In a final step, the clustering algorithm DBSCAN [55] identifies clusters in the reduced state space that correspond to different crystal configurations. This routine assigns each image of the recorded series to a crystal configuration whose occurrence over time is analyzed.

Figure 5 illustrates the procedure for a set of $N_P = 4100$ pictures of a 91-ion crystal recorded with an exposure time of 100 ms each. In Fig. 5(a), each image is represented by a point defined by its three most important coefficients c_{ij}, $i \in \{1, 2, 3\}$. Colors are used to indicate the cluster to which each image has been assigned. The clustering algorithm identifies seven different crystal configurations, shown in Fig. 5(b). These configurations can be represented by the planar graphs shown in Fig. 5(c). The ions form triangular lattices with a certain number of defects that account for the fact that the distance between neighboring ions increases the further the ions are from the crystal center. For each configuration, we determine the probability p_i of observing it by counting the number of images N_i assigned to its cluster and normalizing it, $p_i = N_i/N_P$. In this data set, the main configuration is found with $\max(p_i) < 0.5$, which might seem problematic for quantum simulation experiments for which the crystal always has to be prepared in the same configuration. It is, however, possible to substantially increase this number by fine-tuning the trapping potential such that the energy gap between the ground-state structural configuration and metastable ones increases. To this end, we vary the ratio of oscillation frequencies, $\xi = \omega_y/\omega_z$, along the two weakly

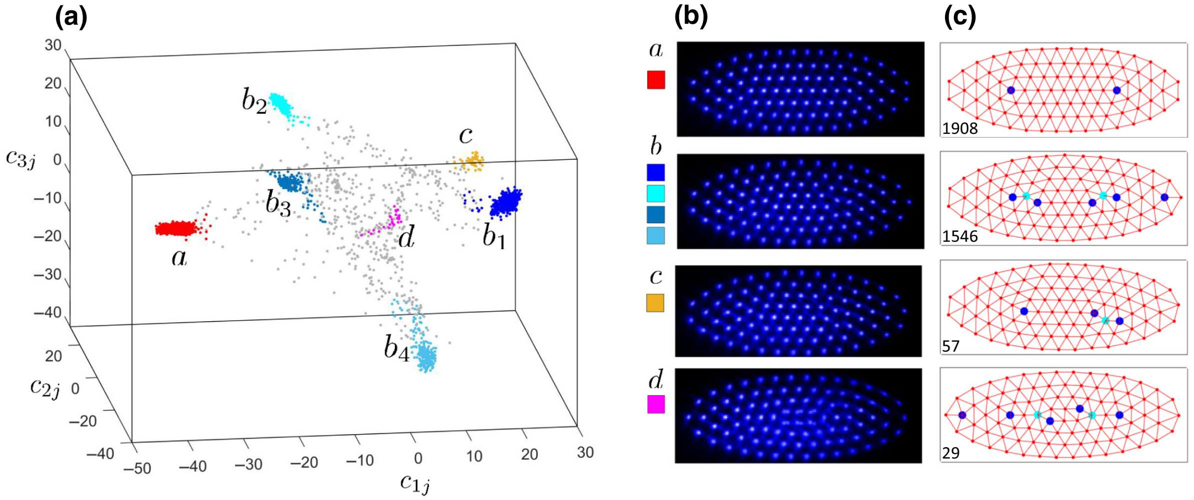

FIG. 5. Configuration analysis of a 91-ion crystal using 4100 camera images. (a) Each image is represented as a point in state space spanned by the projection coefficients c_{ij}. Only the coordinates corresponding to the three highest eigenvalues are plotted. The clustering algorithm identifies seven different clusters (a, b_1–b_4, c, and d). Points are colored depending on their cluster label. Gray points are unlabeled and correspond to images where the ions are hot or undergoing a configuration change during the image acquisition time. (b) Crystal configurations representing the cluster centers. Cluster configurations b_i can be converted into each other by sign flips of the picture coordinates. In the images of cluster d, some of the central ions appear blurred, an effect that we attribute to hot in-plane vibrational modes at low frequencies, or to fast transitions between two (near-)degenerate nonequilibrium configurations during imaging [53]. (c) Each configuration can be represented by a planar graph whose vertices represent ions and whose edges link nearest neighbors. The ions form a triangular lattice with some defects where ions have five or seven neighbors. These defects are plotted as dark blue and light blue vertices, respectively. The number of images found in one of the four configurations is indicated in the lower-left corner.

confining directions with the goal of maximizing p_i for the main configuration. Figure 6(a) displays measurements of p as a function of the trap anisotropy, showing that for $\xi = 1.987$, configuration a is found in more than 99% of the images. Note that in contrast to the case of barely two-dimensional zigzag ion crystals, where there are two degenerate ground-state configurations, there is only a single ground state because of the mirror symmetries of this crystal configuration.

3. Crystal configuration simulations

To better understand how the anisotropy of the trapping potential influences the probability of observing the main configuration, we numerically search for the ground-state and low-energy metastable configurations. In these simulations, we assume that the ions are confined in a conservative anisotropic harmonic potential characterized by oscillation frequencies ω_i and perform an annealing routine with parameters set such that the lowest-energy configuration would be found in about 15% of the annealing runs. For six values of trap anisotropy in the range $1.9 \le \xi \le 2.06$, the annealing procedure is performed 500 times for each value to identify a large number of metastable configurations. In a second step, the configurations found at a particular anisotropy are used as the starting point for an annealing scheme at a slightly different anisotropy using a slower annealing schedule to complete the picture.

We find that the lattice configurations observed in the experiment can be assigned to low-energy configurations obtained by simulated annealing. In Fig. 6(b), we plot the energy gap of these configurations above the energy of the ground-state configuration versus the anisotropy ξ of the potential. All configurations observed in the experiment at $\xi = 1.987$ are found in the simulation, as are the most frequent configurations at $\xi = 1.915$, labeled "a" and "b" in Fig. 5. Moreover, the energy gap between the ground state and the first excited state is nearly at its maximum at $\xi = 1.987$, where the ground-state configuration exhibits the highest stability in the experiment. Here the energy gap corresponds to a temperature of 200 mK. In contrast, at $\xi = 1.915$, the gap is only about 50 mK, which suggests that insufficient laser cooling or low-energy Langevin collisions could induce configuration changes much more easily.

4. Mitigation of configuration changes

The higher stability of the main configuration compared with other configurations is based on the fact that the ion crystal is symmetric with respect to both axes that span the crystal plane, which can be seen in the top image in Figs. 5(b) and 5(c). For given trapping parameters, only

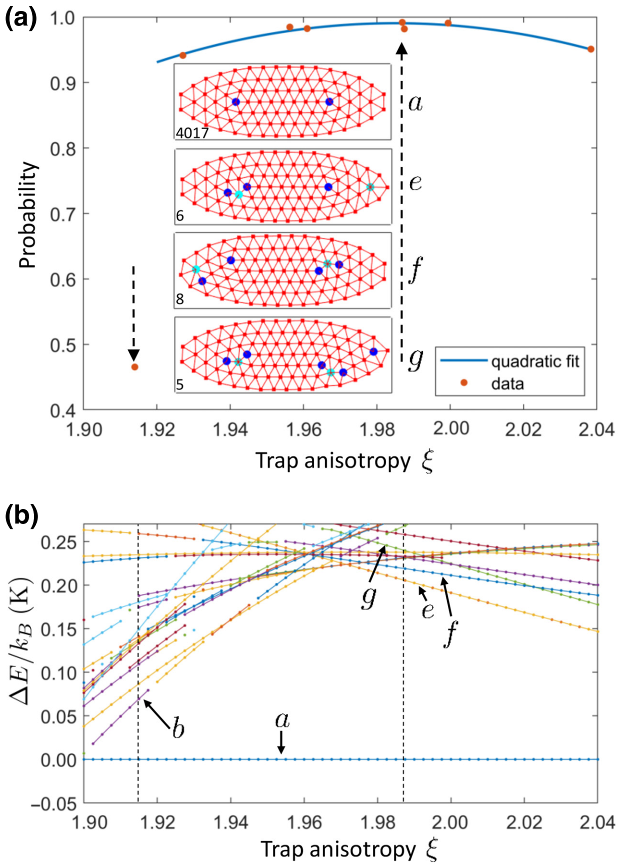

FIG. 6. Crystal configurations versus potential anisotropy for a 91-ion crystal. (a) The red points represent experimental data for the probability of finding the main configuration, $\max(p_i)$, as a function of trap anisotropy ξ. The blue line, a quadratic fit, provides a guide for the eye for data in the stable regime, where the probability of being in the main configuration exceeds 90%, and can be used to find the optimum anisotropy. After optimization of ξ, the main configuration (labeled "a") is found in more than 99% of all 4050 images taken (upward-pointing arrow), whereas configurations e–g are observed only a few times, as indicated by the numbers next to them. The downward-pointing arrow indicates the value of ξ for which the data in Fig. 5 are taken. (b) Numerical simulations of metastable configurations reproduce many configurations found in the experiment. Moreover, they show that the energy gap between metastable configurations and the ground state becomes maximal close to the value of ξ for which the crystal lattice is stablest in the experiment.

crystals consisting of a certain number of ions can fulfill this criterion, which is why we trap specifically 8, 54, 91, and 105 ions, a selection of the possibilities, for the experiments presented in this paper. These particular numbers are found empirically as performing simulations for various trap anisotropies and ion numbers to find stable configurations is impractical.

After the potential anisotropy is fine-tuned to maximize the time spent in the main configuration, the lifetime of metastable configurations is rather short, often not exceeding 10 ms. The effect of undesired transitions into these configurations can then be mitigated in experiments, probing the desired configuration by the experiment control program: it detects the crystal configuration found in each experiment and automatically repeats those experiments where the crystal was found in the wrong configuration. Additionally, it might be feasible to deliberately destabilize an undesired metastable configuration by transiently changing the laser cooling parameters, which has not been necessary for the experiments we have conducted so far.

Low energetic background gas collisions may lead to swapping of ion positions without melting the crystal or changing the crystal lattice structure. Such position changes cannot be detected by the strategies we present in this paper. However, these events are rare, and we estimate their contribution to measurement errors to be well below 10^{-3}.

E. Ground-state cooling of the out-of-plane motional modes

Controlling a large number of ions necessitates fast multimode cooling techniques such as EIT cooling [56] as subsequent cooling of individual modes by Raman or resolved-sideband cooling becomes time-consuming and thus infeasible. EIT cooling, like sideband cooling, is applicable only to precooled ions and has been demonstrated with a single ion [57], long strings of ions [58], 2D crystals in Penning traps [59], and more recently a planar 12-ion crystal in a rf trap [33].

Here we use EIT cooling to prepare all N out-of-plane motional modes of 2D crystals with up to 105 ions close to the ground state. The cooling scheme is implemented in a Λ-type three-level system with use of the Zeeman sublevels of the $4S_{1/2}$ manifold coupled off-resonantly via the $4P_{1/2}$ level. We use two perpendicular beams at 397 nm, one π-polarized beam and one σ^--polarized beam, each having a k vector at an angle of 45° with respect to the crystal plane. The σ^--polarized light strongly couples the $4S_{1/2}$ $(m=+1/2)$ ground state to the $4P_{1/2}$ $(m=-1/2)$ excited state, resulting in the generation of dressed states. The weak π-polarized probe beam couples the $4S_{1/2}$ $(m=-1/2)$ state to the $4P_{1/2}$ $(m=-1/2)$ state and probes the resulting Fano-like absorption spectrum. The light shift from the bare energy states is adjusted via the power of the σ^--polarized beam to match the center of the out-of-plane frequency spectrum, spanning a few hundred kilohertz. This ensures that all mode frequencies are covered by the absorption spectrum to enable efficient cooling of all modes simultaneously.

To verify that all motional modes are cooled, we perform frequency scans probing the red-sideband spectrum of the $4S_{1/2} \leftrightarrow 3D_{5/2}$ transition, once after only Doppler cooling, and once after additional EIT cooling for 300 μs

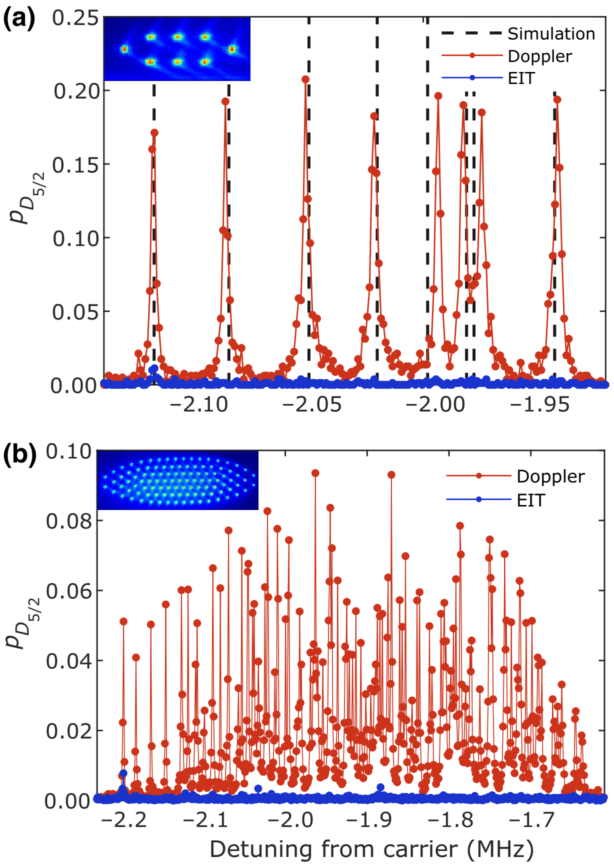

FIG. 7. EIT cooling of (a) an eight-ion crystal and (b) a 105-ion crystal. The red data points represent the red-sideband excitation spectrum of the out-of-plane modes after only Doppler cooling and the blue data points represent the red-sideband excitation spectrum of the out-of-plane modes with additional EIT cooling for 300 μs. The most prominent peaks in the EIT-cooled spectra are the center-of-mass modes, which heat up during the measurement time in proportion to $\dot{\bar{n}}N$. Note that the solid red and blue lines are guides for the eye. The dashed vertical lines in (a) show the simulated mode frequencies for the given trapping parameters obtained from pseudopotential theory.

and optical pumping for 100 μs. Figure 7 shows the measured spectra for an eight-ion crystal trapped in a potential with oscillation frequencies $\omega_x = 2\pi \times 2118$ kHz, $\omega_y = 2\pi \times 702$ kHz, and $\omega_z = 2\pi \times 370$ kHz, and for a 105-ion crystal trapped in a potential with oscillation frequencies $\omega_x = 2\pi \times 2188$ kHz, $\omega_y = 2\pi \times 528$ kHz, and $\omega_z = 2\pi \times 248$ kHz.

In the Doppler-cooled spectrum we identify the red sidebands of the out-of-plane motional modes. For the eight-ion crystal, the mode frequencies as well as the mode structure represented by the Lamb-Dicke parameters of individual ions are obtained by numerical simulations based on pseudopotential theory and are compared with the experimental data. For most of the modes we find good agreement between the simulated values and the measured mode frequencies as well as relative couplings to individual ions in a planar crystal. To understand the deviations for some of the modes at lower frequencies, we perform further simulations using a Floquet-Lyapunov approach [60] as well as a Fourier transform of the simulated motion of the ions, both of which take the full rf field into account. However, neither of the methods improves the agreement between simulated and measured normal mode frequencies. The reason for the discrepancies is unknown. These deviations do not necessarily scale with the number of ions as we have already observed better matches for all out-of-plane modes of larger crystals (e.g., 19 ions).

In the EIT-cooled spectra we see a clear suppression of excitation for all out-of-plane motional modes, which demonstrates an efficient ground-state cooling in a qualitative way. A quantitative investigation of such low temperatures is not straightforward, as standard methods applicable to single ions are not directly adaptable for large ion crystals. A generalized sideband thermometry technique applicable to individual modes in larger crystals has been studied and will be the subject of a forthcoming publication.

Least-squares fits of Rabi oscillations of the red sideband of the center-of-mass mode in an eight-ion crystal, as well as sideband thermometry of a single ion [61], revealed a mean phonon number $\bar{n}$ of the out-of-plane center-of-mass mode of 0.06 quanta after EIT cooling. Introducing a variable waiting time between EIT cooling and the temperature measurement provided a heating rate $\dot{\bar{n}}$ of about 15 quanta per second per ion for the center-of-mass mode, which experiences the highest degree of heating among all out-of-plane modes. This value is not competitive with some of the lowest heating rates reported in the literature [62,63], but might be improved by a change of the design of the dc filter lines, potentially reducing the electronic noise level on the dc electrodes.

IV. CONCLUSION

In this work, we present an ion-trap apparatus developed with the goal of conducting quantum simulations for studying 2D many-body physics beyond the capabilities of classical computers. The characterization measurements provided in this paper reflect the high level of control we achieve in our setup, providing a solid foundation for the planned endeavors. Fundamental requirements for the envisaged experiments include the ability to trap large ion crystals that extend in two dimensions only (to minimize adverse micromotion-induced effects on laser-ion interactions) and to ensure a stable crystal lattice during measurements.

Our apparatus is capable of trapping stationary, 2D crystals of approximately 100 ions. We achieve planarity via voltage control of the trap dc electrodes and verify it by measuring low out-of-plane micromotion modulation indices. We find excellent ion-crystal stability from the observed typical crystal lifetimes of several hours, survival in crystalline form for at least several seconds in the absence of any laser cooling, and fast, automated, recrystallization (approximately 100 ms) once a melting event occurs. Moreover, we demonstrate that the influence of crystal lattice configuration changes on experiments can be practically eliminated, disarming a major challenge when one is working with large 2D crystals. To this end, lattice instabilities are minimized by adjustment of the trap anisotropy. In addition, data are automatically retaken for rare remaining occurrences of structural changes after in-sequence identification of the crystal configuration. A stable planar 91-ion crystal has already been used successfully for correlation spectroscopy measurements reported in Ref. [15], demonstrating the experimental robustness of our apparatus.

Another requirement for the planned quantum simulation experiments is precise knowledge and high control of the crystals' out-of-plane motional modes, as they will be used to mediate entangling interactions between the ions. First, anharmonicities in the trapping potential could lead to a modification of the normal-mode frequencies and amplitudes [64]. From the analysis of crystal images, we find that substantial contributions from anharmonicities to the trapping potential can be ruled out. Second, cooling of these modes close to the motional ground state has to be achieved. We present EIT cooling of a small (eight-ion) crystal and a large (105-ion) crystal. Compared with previously reported results on ground-state cooling of linear and 2D crystals held in rf traps, our results represent an improvement by a factor of 2 and an order of magnitude, respectively, in terms of ion number. Third, we find sufficient stability of the motional modes, a prerequisite for creating reliable entangling interactions, from observing low drifts and a heating-rate-limited motional coherence.

To create entangling interactions, we are currently setting up a laser system at 396 nm to couple the ground-state qubit on a stimulated Raman transition via the excited $4P_{1/2}$ and $4P_{3/2}$ states. By using a bichromatic light field, detuned from the red and blue sidebands of the out-of-plane motional modes of the crystal, we will be able to engineer spin-spin interactions with a tunable interaction strength [65]. Here we estimate the dominant error source to be spontaneous Raman scattering, which can be kept at low levels by detuning the laser far off resonance from both the $4S_{1/2} \leftrightarrow 4P_{1/2}$ transition and the $4S_{1/2} \leftrightarrow 4P_{3/2}$ transition. Entangling interactions might also be affected by motional heating, which we anticipate will be reduced by a change of low-pass filters on the trap dc electrodes.

Moreover, we aim to implement individual-ion control via a tightly focused 729-nm laser beam steered by a 2D acousto-optic deflector. This will enable sequential single-qubit rotations and structuring of the crystal lattice into different geometries by shelving ions into long-lived states that do not couple to the field, inducing spin-spin interactions. Provided that the laser pulse duration is long (e.g., 10 μs) compared with the period of the rf drive (approximately 23 ns), errors due to the ion experiencing a micromotion-induced amplitude modulation of the laser intensity are negligible.

ACKNOWLEDGMENTS

We thank Mark Dugan and Philippe Bado from Translume Inc., Alpine Quantum Technologies GmbH, and the Innsbruck ion trapping research groups for their support. This project has received funding from the European Research Council under the European Union's Horizon 2020 research and innovation program (Grant Agreement No. 741541). Furthermore, we acknowledge funding from the European Union's Horizon 2020 research and innovation program under Marie Skłodowska–Curie Grant Agreement No. 801110 and the Austrian Federal Ministry of Education, Science and Research.

D.K. and H.H. contributed equally to this work.

APPENDIX A: COMPARISON OF DIFFERENT CRYSTAL ORIENTATIONS

We compare the creation of planar ion crystals in a linear rf trap in two different geometries. First, we consider an ion crystal that is trapped in a plane spanned by the two radial trap directions. Second, we consider a crystal in the plane spanned by one radial direction and the axial trap direction. We compare these two cases in terms of rf-power requirements as well as stability of the trap frequencies in the weakly confined directions in the presence of rf-power fluctuations. Lower stability can lead to more crystal lattice configuration changes, which should be suppressed as much as possible.

We assume that one wants to trap the crystal in a potential characterized by the three secular frequencies ω_i. Moreover, the q parameter should be upper-bounded by a value q_m to keep the micromotion amplitude low. The following calculation is done within the pseudopotential approximation.

In a linear trap, the oscillation frequencies can be expressed in terms of the q and a parameters and the trap drive frequency Ω:

$$\omega_i = \frac{\Omega}{2}\sqrt{\frac{q^2}{2} + a_i}, \quad i \in 1, 2, \tag{A1}$$

$$\omega_3 = \frac{\Omega}{2}\sqrt{a_3}, \tag{A2}$$

with $a_1 + a_2 + a_3 = 0$, where a_i are set by static voltages. Because $\sum_n \omega_n^2 = q^2\Omega^2/4$, this lower-bounds the value of the angular drive frequency Ω to

$$\Omega^2 = \frac{4}{q^2}\sum_{n=1}^{3}\omega_n^2 \geq \frac{4}{q_m^2}\sum_{n=1}^{3}\omega_n^2. \tag{A3}$$

As Eq. (A3) does not depend on the orientation of the planar crystal in the trap, the minimum rf power required to generate the desired set of secular frequencies is the same for both geometries.

Secondly, we investigate the influence of trap-voltage fluctuations on the secular frequencies. As it is much harder to generate stable rf voltages than stable dc voltages, we focus on the influence of rf-power fluctuations, which will change the q parameter. The secular frequencies depend on q via

$$\frac{d\omega_i}{dq} = \frac{\Omega}{4}\frac{q}{\sqrt{\frac{q^2}{2}+a_i}} = \frac{\Omega^2 q}{8\omega_i} = \frac{1}{2q\omega_i}\sum_{n=1}^{3}\omega_n^2, \quad i \in 1, 2, \tag{A4}$$

$$\frac{d\omega_3}{dq} = 0. \tag{A5}$$

For the realization of spin-spin interactions, the lasers are typically detuned by a few tens of kilohertz from the center-of-mass mode with the highest frequency. In view of suppressing the coupling strength variations caused by fluctuating rf voltages, the best option is to confine the crystal in the radial plane of the linear trap. However, Eq. (A4) shows that for a crystal whose plane includes the axial direction, the effect of fluctuating trap voltages on the detuning of the bichromatic beam is about 2 times weaker than for the case of an ion string in a linear trap with the same maximum secular frequency. A second point to be considered is changes in the aspect ratio of a planar crystal induced by fluctuating rf voltages V_{rf}. For a planar crystal of circular shape trapped in the radial plane, the aspect ratio does not change. For a crystal aligned with the axial direction, the oscillation frequency of the weak axis that is pointing into the radial direction is affected, leading to changes of the trap anisotropy ξ. A rf-voltage change ΔV_{rf} will change ξ as

$$\frac{\Delta\xi}{\xi} = -\left(\frac{\Delta V_{\text{rf}}}{V_{\text{rf}}}\right)\frac{\sum_n \omega_n^2}{2\omega_2^2}$$

if $\omega_1 \gg \omega_2 \geq \omega_3$. This shows that ξ is more sensitive to changes of V_{rf} than ω_1. Therefore, care should be taken to actively stabilize the rf voltage.

APPENDIX B: TECHNICAL DETAILS OF THE ION TRAP

1. Ion trap geometry

We optimize the electrode structure of the ion trap using finite-element simulations (COMSOL MULTIPHYSICS) to best fulfill the constraints imposed by the envisaged quantum simulation experiments. Here, in particular, it is important to create sufficiently fast interactions, which rely on high secular frequencies. We aim for a secular frequency of 2 MHz in the strongly confined direction. Additionally, it is beneficial to have $q < 0.1$ as the micromotion amplitude scales linearly with q. The q parameter and secular frequencies relate to the trap drive frequency, the rf voltage that is applied to the trap, and the distance between the ions and the trap electrodes. There exists a limit to how much voltage the trap chip can reasonably handle, which we estimate to be on the order of 1 kV peak to peak. The aforementioned constraints for the desired secular frequencies, q, and maximum rf drive voltage already put a bound on the rf drive frequency, which can be chosen by design of the helical resonator circuit that is used to amplify the trap rf voltage. To reduce anomalous heating of the ions [66], it is beneficial to keep the distance between ions and the trap electrode as large as possible. From simulations we find a trade-off between all parameters and end up with a distance d of 400 μm between the rf electrode and trap center.

The length of the central dc electrode segments of the trap is chosen on the basis of the ability to perform tilting operations on the ion crystals with respect to the principal axes. A length of 1.5 mm is short enough to allow efficient tilting via reasonably low asymmetric voltages on the outer dc segments.

2. Control and stability of the trap rf

To produce the high-voltage rf field required to drive the trap, we amplify the signal from a frequency generator with a rf amplifier as well as a helical resonator [67]. The resonance frequency depends on the circuit's inductance, dominated by its coil (40.4-mm diameter, 5-mm wire thickness, 10-mm winding pitch, and 70-mm coil height), and capacitance, dominated by the trap itself. We find a resonance at 43.22 MHz, from which we estimate the upper limit for the capacitance of the trap to be about 12 pF.

Without active stabilization, we observe typical drifts of the radial frequencies of several kilohertz over a timescale of minutes, caused by temperature fluctuations around the experiment, which need to be corrected for. A homebuilt circuit based on a proportional-integral controller is used to stabilize the rf power. The input signal for the circuit is detected inductively with a pickup coil close to the coil of the helical resonator. Spectroscopic measurements on a single ion reveal that for a secular frequency $\omega_x = 2\pi \times 2.25$ MHz the peak-to-peak variation of the oscillation frequency is below 100 Hz over the course of 1 h, with the main variation being given by a linear drift. Moreover, Ramsey experiments on motional superposition states $|0\rangle + |1\rangle$ yield a coherence time of about 40 ms that is limited by motional heating. The combination of these two measurements demonstrates that the rf stabilization provides excellent frequency stability on both long and short timescales.

3. Trapping potential shaping and micromotion compensation

The shape of the trapping potential can be precisely controlled via the 12 segmented dc electrodes of the ion trap. Low-pass filters (first order) with cutoff frequencies of about 300 Hz are used to suppress noise in the secular frequency regime while allowing the possibility of fast dc voltage control on millisecond timescales.

To execute certain actions on the ion crystals, such as micromotion compensation (shifts in x, y, or z), rotation of the potential (about the x, y, or z axis), or adjustment of the confinement along one of the three principle axes, we calculate the required voltages that are applied to the 12 dc electrodes to implement these actions. A fit to the trap potential of the individual electrodes obtained from finite-element simulations, done in COMSOL MULTIPHYSICS based on our trap design, forms the basis for these calculations. The trap potential of each electrode is expanded into spherical harmonic terms. In this way, the various actions on the ion crystal can be decoupled from each other. In a second step, an overdetermined inversion problem has to be solved linking the required action on the ions to the voltages that need to be applied on all 12 dc electrodes as described in Appendix B in Ref. [68]. We use the Tikhonov method to solve the equations based on a singular value decomposition [69].

[1] J. Preskill, Quantum computing in the NISQ era and beyond, Quantum **2**, 79 (2018).

[2] I. Buluta and F. Nori, Quantum simulators, Science **326**, 108 (2009).

[3] J. R. McClean, J. Romero, R. Babbush, and A. Aspuru-Guzik, The theory of variational hybrid quantum-classical algorithms, New J. Phys. **18**, 023023 (2016).

[4] C. Gross and I. Bloch, Quantum simulations with ultracold atoms in optical lattices, Science **357**, 995 (2017).

[5] C. Monroe, W. C. Campbell, L.-M. Duan, Z.-X. Gong, A. V. Gorshkov, P. W. Hess, R. Islam, K. Kim, N. M. Linke, G. Pagano, P. Richerme, C. Senko, and N. Y. Yao, Programmable quantum simulations of spin systems with trapped ions, Rev. Mod. Phys. **93**, 025001 (2021).

[6] A. Browaeys and T. Lahaye, Many-body physics with individually controlled Rydberg atoms, Nat. Phys. **16**, 132 (2020).

[7] F. Arute, *et al.*, Hartree-Fock on a superconducting qubit quantum computer, Science **369**, 1084 (2020).

[8] A. Morvan, *et al.*, Formation of robust bound states of interacting microwave photons, Nature **612**, 240 (2022).

[9] A. Aspuru-Guzik and P. Walther, Photonic quantum simulators, Nat. Phys. **8**, 285 (2012).

[10] J. Wang, F. Sciarrino, A. Laing, and M. G. Thompson, Integrated photonic quantum technologies, Nat. Photonics **14**, 273 (2020).

[11] C. Figgatt, A. Ostrander, N. M. Linke, K. A. Landsman, D. Zhu, D. Maslov, and C. Monroe, Parallel entangling operations on a universal ion-trap quantum computer, Nature **572**, 368 (2019).

[12] L. Postler, S. Heußen, I. Pogorelov, M. Rispler, T. Feldker, M. Meth, C. D. Marciniak, R. Stricker, M. Ringbauer, R. Blatt, P. Schindler, M. Müller, and T. Monz, Demonstration of fault-tolerant universal quantum gate operations, Nature **605**, 675 (2022).

[13] S. M. Brewer, J.-S. Chen, A. M. Hankin, E. R. Clements, C. W. Chou, D. J. Wineland, D. B. Hume, and D. R. Leibrandt, ^{27}Al^{+} Quantum-Logic Clock with a Systematic Uncertainty below 10^{-18}, Phys. Rev. Lett. **123**, 033201 (2019).

[14] C. D. Marciniak, T. Feldker, I. Pogorelov, R. Kaubruegger, D. V. Vasilyev, R. van Bijnen, P. Schindler, P. Zoller, R. Blatt, and T. Monz, Optimal metrology with programmable quantum sensors, Nature **603**, 604 (2022).

[15] H. Hainzer, D. Kiesenhofer, T. Ollikainen, M. Bock, F. Kranzl, M. K. Joshi, G. Yoeli, R. Blatt, T. Gefen, and C. F. Roos, Correlation spectroscopy with multi-qubit-enhanced phase estimation, ArXiv:2203.12656 (2022).

[16] R. Blatt and C. F. Roos, Quantum simulations with trapped ions, Nat. Phys. **8**, 277 (2012).

[17] J. Zhang, G. Pagano, P. W. Hess, A. Kyprianidis, P. Becker, H. Kaplan, A. V. Gorshkov, Z.-X. Gong, and C. Monroe, Observation of a many-body dynamical phase transition with a 53-qubit quantum simulator, Nature **551**, 601 (2017).

[18] C. Kokail, C. Maier, R. van Bijnen, T. Brydges, M. K. Joshi, P. Jurcevic, C. A. Muschik, P. Silvi, R. Blatt, C. F. Roos, and P. Zoller, Self-verifying variational quantum simulation of lattice models, Nature **569**, 355 (2019).

[19] M. K. Joshi, F. Kranzl, A. Schuckert, I. Lovas, C. Maier, R. Blatt, M. Knap, and C. F. Roos, Observing emergent hydrodynamics in a long-range quantum magnet, Science **376**, 720 (2022).

[20] B.-W. Li, Y.-K. Wu, Q.-X. Mei, R. Yao, W.-Q. Lian, M.-L. Cai, Y. Wang, B.-X. Qi, L. Yao, L. He, Z.-C. Zhou, and L.-M. Duan, Probing Critical Behavior of Long-Range Transverse-Field Ising Model through Quantum Kibble-Zurek Mechanism, PRX Quantum **4**, 010302 (2023).

[21] F. Kranzl, M. K. Joshi, C. Maier, T. Brydges, J. Franke, R. Blatt, and C. F. Roos, Controlling long ion strings for quantum simulation and precision measurements, Phys. Rev. A **105**, 052426 (2022).

[22] J. P. Schiffer, Phase Transitions in Anisotropically Confined Ionic Crystals, Phys. Rev. Lett. **70**, 818 (1993).

[23] D. H. E. Dubin, Theory of Structural Phase Transitions in a Trapped Coulomb Crystal, Phys. Rev. Lett. **71**, 2753 (1993).

[24] J. G. Bohnet, B. C. Sawyer, J. W. Britton, M. L. Wall, A. M. Rey, M. Foss-Feig, and J. J. Bollinger, Quantum spin dynamics and entanglement generation with hundreds of trapped ions, Science **352**, 1297 (2016).

[25] A. M. Polloreno, A. M. Rey, and J. J. Bollinger, Individual qubit addressing of rotating ion crystals in a Penning trap, Phys. Rev. Res. **4**, 033076 (2022).

[26] R. C. Sterling, H. Rattanasonti, S. Weidt, K. Lake, P. Srinivasan, S. C. Webster, M. Kraft, and W. K. Hensinger, Fabrication and operation of a two-dimensional ion-trap lattice on a high-voltage microchip, Nat. Commun. **5**, 3637 (2014).

[27] M. Mielenz, H. Kalis, M. Wittemer, F. Hakelberg, U. Warring, R. Schmied, M. Blain, P. Maunz, D. L. Moehring, D. Leibfried, and T. Schaetz, Arrays of individually controlled ions suitable for two-dimensional quantum simulations, Nat. Commun. **7**, 11839 (2016).

[28] P. C. Holz, S. Auchter, G. Stocker, M. Valentini, K. Lakhmanskiy, C. Rössler, P. Stampfer, S. Sgouridis, E. Aschauer, Y. Colombe, and R. Blatt, 2D linear trap array for quantum information processing, Adv. Quantum Technol. **3**, 2000031 (2020).

[29] B. Yoshimura, M. Stork, D. Dadic, W. C. Campbell, and J. K. Freericks, Creation of two-dimensional Coulomb crystals of ions in oblate Paul traps for quantum simulations, EPJ Quantum Technol. **2**, 2 (2015).

[30] Y. Wang, M. Qiao, Z. Cai, K. Zhang, N. Jin, P. Wang, W. Chen, C. Luan, B. Du, H. Wang, Y. Song, D. Yum, and K. Kim, Coherently manipulated 2D ion crystal in a monolithic Paul trap, Adv. Quantum Technol. **3**, 2000068 (2020).

[31] M. K. Ivory, A. Kato, A. Hasanzadeh, and B. B. Blinov, A Paul trap with sectored ring electrodes for experiments with two-dimensional ion crystals, Rev. Sci. Instrum. **91**, 053201 (2020).

[32] Y. Xie, J. Cui, M. D'Onofrio, A. J. Rasmusson, S. W. Howell, and P. Richerme, An open-endcap blade trap for radial-2D ion crystals, Quantum Sci. Technol. **6**, 044009 (2021).

[33] M. Qiao, Y. Wang, Z. Cai, B. Du, P. Wang, C. Luan, W. Chen, H.-R. Noh, and K. Kim, Double-Electromagnetically-Induced-Transparency Ground-State Cooling of Stationary Two-Dimensional Ion Crystals, Phys. Rev. Lett. **126**, 023604 (2021).

[34] M. Qiao, Z. Cai, Y. Wang, B. Du, N. Jin, W. Chen, P. Wang, C. Luan, E. Gao, X. Sun, H. Tian, J. Zhang, and K. Kim, Observing frustrated quantum magnetism in two-dimensional ion crystals, ArXiv:2204.07283 (2022).

[35] M. Block, A. Drakoudis, H. Leuthner, P. Seibert, and G. Werth, Crystalline ion structures in a Paul trap, J. Phys. B **33**, L375 (2000).

[36] R. Blümel, C. Kappler, W. Quint, and H. Walther, Chaos and order of laser-cooled ions in a Paul trap, Phys. Rev. A **40**, 808 (1989).

[37] L. Deslauriers, P. C. Haljan, P. J. Lee, K.-A. Brickman, B. B. Blinov, M. J. Madsen, and C. Monroe, Zero-point cooling and low heating of trapped $^{111}\mathrm{Cd}^{+}$ ions, Phys. Rev. A **70**, 043408 (2004).

[38] F. v. Busch and W. Paul, Über nichtlineare Resonanzen im elektrischen Massenfilter als Folge von Feldfehlern, Z. Phys. **164**, 588 (1961).

[39] R. Alheit, S. Kleineidam, F. Vedel, M. Vedel, and G. Werth, Higher order non-linear resonances in a Paul trap, Int. J. Mass Spectrom. **154**, 155 (1996).

[40] R. B. Blakestad, Ph.D. thesis, University of Colorado, 2010.

[41] Translume Inc., Ann Arbor, Michigan 48108, USA.

[42] P. Bado, C. R. Monroe, and W. C. Campbell, Fused silica ion trap chip with efficient optical collection system for timekeeping, sensing, and emulation, 2015. https://apps.dtic.mil/sti/citations/ADA619271.

[43] C. Noel, M. Berlin-Udi, C. Matthiesen, J. Yu, Y. Zhou, V. Lordi, and H. Häffner, Electric-field noise from thermally activated fluctuators in a surface ion trap, Phys. Rev. A **99**, 063427 (2019).

[44] S. Ragg, C. Decaroli, T. Lutz, and J. P. Home, Segmented ion-trap fabrication using high precision stacked wafers, Rev. Sci. Instrum. **90**, 103203 (2019).

[45] C. Decaroli, R. Matt, R. Oswald, C. Axline, M. Ernzer, J. Flannery, S. Ragg, and J. P. Home, Design, fabrication and characterization of a micro-fabricated stacked-wafer segmented ion trap with two x-junctions, Quantum Sci. Technol. **6**, 044001 (2021).

[46] G. Araneda, G. Cerchiari, D. B. Higginbottom, P. C. Holz, K. Lakhmanskiy, P. Obšil, Y. Colombe, and R. Blatt, The panopticon device: An integrated Paul-trap-hemispherical mirror system for quantum optics, Rev. Sci. Instrum. **91**, 113201 (2020).

[47] H. Kaufmann, S. Ulm, G. Jacob, U. Poschinger, H. Landa, A. Retzker, M. B. Plenio, and F. Schmidt-Kaler, Precise Experimental Investigation of Eigenmodes in a Planar Ion Crystal, Phys. Rev. Lett. **109**, 263003 (2012).

[48] O. D. Kellogg, *Foundations of Potential Theory* (Springer Berlin Heidelberg, 2013).

[49] D. H. E. Dubin and T. M. O'Neil, Trapped nonneutral plasmas, liquids, and crystals (the thermal equilibrium states), Rev. Mod. Phys. **71**, 87 (1999).

[50] M. W. van Mourik, P. Hrmo, L. Gerster, B. Wilhelm, R. Blatt, P. Schindler, and T. Monz, rf-induced heating dynamics of noncrystallized trapped ions, Phys. Rev. A **105**, 033101 (2022).

[51] R. Blümel, J. M. Chen, E. Peik, W. Quint, W. Schleich, Y. R. Shen, and H. Walther, Phase transitions of stored laser-cooled ions, Nature **334**, 309 (1988).

[52] S. Fishman, G. De Chiara, T. Calarco, and G. Morigi, Structural phase transitions in low-dimensional ion crystals, Phys. Rev. B **77**, 064111 (2008).

[53] L. Yan, W. Wan, L. Chen, F. Zhou, S. Gong, X. Tong, and M. Feng, Exploring structural phase transitions of ion crystals, Sci. Rep. **6**, 21547 (2016).

[54] V. L. Ryjkov, X. Zhao, and H. A. Schuessler, Simulations of the rf heating rates in a linear quadrupole ion trap, Phys. Rev. A **71**, 033414 (2005).

[55] M. Ester, H.-P. Kriegel, J. Sander, and X. Xu, in *Proceedings of the Second International Conference on Knowledge Discovery and Data Mining*, KDD'96 (AAAI Press, Portland, Oregon, 1996), p. 226.

[56] G. Morigi, J. Eschner, and C. H. Keitel, Ground State Laser Cooling Using Electromagnetically Induced Transparency, Phys. Rev. Lett. **85**, 4458 (2000).

[57] C. F. Roos, D. Leibfried, A. Mundt, F. Schmidt-Kaler, J. Eschner, and R. Blatt, Experimental Demonstration of Ground State Laser Cooling with Electromagnetically Induced Transparency, Phys. Rev. Lett. **85**, 5547 (2000).

[58] R. Lechner, C. Maier, C. Hempel, P. Jurcevic, B. P. Lanyon, T. Monz, M. Brownnutt, R. Blatt, and C. F. Roos, Electromagnetically-induced-transparency ground-state cooling of long ion strings, Phys. Rev. A **93**, 053401 (2016).

[59] E. Jordan, K. A. Gilmore, A. Shankar, A. Safavi-Naini, J. G. Bohnet, M. J. Holland, and J. J. Bollinger, Near Ground-State Cooling of Two-Dimensional Trapped-Ion Crystals with More Than 100 Ions, Phys. Rev. Lett. **122**, 053603 (2019).

[60] H. Landa, M. Drewsen, B. Reznik, and A. Retzker, Modes of oscillation in radiofrequency Paul traps, New J. Phys. **14**, 093023 (2012).

[61] D. Leibfried, R. Blatt, C. Monroe, and D. Wineland, Quantum dynamics of single trapped ions, Rev. Mod. Phys. **75**, 281 (2003).

[62] D. An, C. Matthiesen, E. Urban, and H. Häffner, Distance scaling and polarization of electric-field noise in a surface ion trap, Phys. Rev. A **100**, 063405 (2019).

[63] I. Pogorelov, T. Feldker, C. D. Marciniak, L. Postler, G. Jacob, O. Krieglsteiner, V. Podlesnic, M. Meth, V. Negnevitsky, M. Stadler, B. Höfer, C. Wächter, K. Lakhmanskiy, R. Blatt, P. Schindler, and T. Monz, Compact Ion-Trap Quantum Computing Demonstrator, PRX Quantum **2**, 020343 (2021).

[64] J. P. Home, D. Hanneke, J. D. Jost, D. Leibfried, and D. J. Wineland, Normal modes of trapped ions in the presence of anharmonic trap potentials, New J. Phys. **13**, 073026 (2011).

[65] D. Porras and J. I. Cirac, Effective Quantum Spin Systems with Trapped Ions, Phys. Rev. Lett. **92**, 207901 (2004).

[66] M. Brownnutt, M. Kumph, P. Rabl, and R. Blatt, Ion-trap measurements of electric-field noise near surfaces, Rev. Mod. Phys. **87**, 1419 (2015).

[67] J. D. Siverns, L. R. Simkins, S. Weidt, and W. K. Hensinger, On the application of radio frequency voltages to ion traps via helical resonators, Appl. Phys. B **107**, 921 (2012).

[68] M. W. van Mourik, E. A. Martinez, L. Gerster, P. Hrmo, T. Monz, P. Schindler, and R. Blatt, Coherent rotations of qubits within a surface ion-trap quantum computer, Phys. Rev. A **102**, 022611 (2020).

[69] K. Singer, U. Poschinger, M. Murphy, P. Ivanov, F. Ziesel, T. Calarco, and F. Schmidt-Kaler, Colloquium: Trapped ions as quantum bits: Essential numerical tools, Rev. Mod. Phys. **82**, 2609 (2010).